Fundamentals of grinding

Hegeman, J

Chapter 2

BASIC CONCEPTS

In this chapter, the basic concepts of the grinding process are elaborated. Grinding models will be introduced and in addition, the experimental techniques like confocal scanning optical microscopy, electron microscopy and X-ray diffraction that were used to analyse the results of the real grinding experiments will be described.

2.1 INTRODUCTION

All classes of machining processes have one thing in common: removing unwanted material from the workpiece. Grinding is often used as surface finish after the production of materials and products. Most grinding processes are similar, however, the operation may vary according to the wheel shape, motions, etc. During the process an abrasive surface is pressed against the workpiece and then, by moving either the abrasive surface or the workpiece, material is removed by mechanical action of irregularly shaped abrasive grains in all grinding operations.

In this chapter, first an introduction is given to the overall grinding process and then some basic models of the grinding process are reviewed. Those models were proposed in order to estimate roughness values, grinding energy, wheel wear and grinding forces. Most of the models were based on geometrical assumptions and the kinematics of the grinding process. An important deficiency of those models is the assumption of a uniform distribution of grains on the grinding wheel and the uniform size distribution of the abrasive grains.

The surfaces of ground materials were studied using various techniques. Scanning electron microscopy (Philips XL30FEG SEM) was applied to study the morphology and material removal behaviour. Scanning confocal microscopy was used to study the topography and roughness after the grinding process. X-ray diffraction was employed to determine the mechanically induced residual stresses. Defects at the machined surface were quantified by positron annihilation experiments. Finally, some magnetic measurements were performed to monitor the changes in magnetic properties after grinding.

2.2 GRINDING MODELS AND THEORY

In this section, the basic principles of the grinding process, the grinding machine and grinding models are explained and also the analysis of the ground surface is described.

2.2.1 Basic principles of the grinding process and the grinding machine

The grinding experiments were performed on a Jung JF415 grinding machine for straight/plane surface grinding. The basic setup of such a grinding machine is shown in figure 2.1. The important parts of the machine are the grinding table, grinding wheel, coolant nozzle and controller unit. The specimens are mounted on a magnetic table (2), which can move in the y-direction. The height z is adjusted (4) in such a way that the thickness of the removed layer, i.e. the depth of cut, is fixed relatively to the most protruding grain on the grinding wheel (1). This is done by slowly rotating the wheel and gradually decreasing the distance between the wheel and the workpiece. When the most protruding grain hits the surface, a noise is produced and the level is set. The sample is then centred in x-direction, with respect to the width of the grinding wheel (5).

A magnified impression of the interaction of the grinding wheel with a specimen is presented in figure 2.2. It should be noted that the diameter of the wheel in this figure is not presented in original proportions; in reality, the radius is much larger than the thickness of the removed layer. Essentially, a grinding wheel consists of a large number of abrasive particles, called grains, held together by a suitable agent, the bond. The cutting process of a grinding wheel may be regarded as a multi-interacting cutting tool with a cutting action similar to that of a milling cutter, except that the cutting points are irregularly shaped and are randomly distributed over the wheel surface.

The grinding wheels (with diamond abrasives in a metal or resin binder) are first dressed and then used on waste samples in order to run in the wheel before the actual grinding experiments. This dressing process and the running in of a wheel is important for the stabilisation of wheel wear. During the dressing process, material is removed from the grinding wheel and fresh diamond grains will appear at the surface of the wheel. A freshly dressed grinding wheel contains therefore sharp abrasives that will break during the first use of the wheel. Then the wheel stabilises for a certain time, depending on the grinding load, and at the end of the lifecycle of the grinding wheel, many abrasive grains are worn and blunted. Then it is necessary to dress the wheel again before further use. The grinding experiments are performed during the (statistical) steady state of the grinding wheel.

figure 2.1: *The grinding machine.*

The grinding machine is of the type of the Jung JF series for surface grinding (Jung JF 415) installed at the university of Eindhoven (TU/e). (1) Grinding wheel (2) Mounting table for the specimens (3) Nozzle for the infeed of coolant (4) Adjustment screws for the wheel (5) Position adjustment (6) Controller of the grinding machine. The x, y and z arrows denote the direction of movement of the specimen relative to the grinding wheel.

During the grinding process, a water-oil emulsion is used to cool the specimen. Therefore burnout and thermal damage of the surface layer can be avoided. This coolant can be injected at different positions. For this specific grinding operation, the coolant is injected parallel to the grinding direction at the cutting interface (No 3 in figure 2.1). The specimens are glued on a steel plate with hot wax (dissolvable in acetone) and mounted on the specimen table of the grinding machine (No 2). In order to get a homogeneous depth of cut over the whole surface of the specimen it should be precisely aligned relative to the wheel surface. Throughout this thesis, a single pass surface grinding is used for the grinding experiments. However, most relations can be generalised to other grinding configurations.

The main parameters that are varied in order to control the surface quality of the ground specimens are indicated in figure 2.2. The depth of cut d_{cut}, i.e. the thickness of the removed layer, is a parameter that controls the material removal behaviour of the specimen. The ratio between the rotational speed v_{s} of the grinding wheel and the translational speed of the workpiece v_{w} can be optimized for surface roughness, but also for the total energy input used for grinding and for thermal effects (burn out, surface melting) on the specimens.

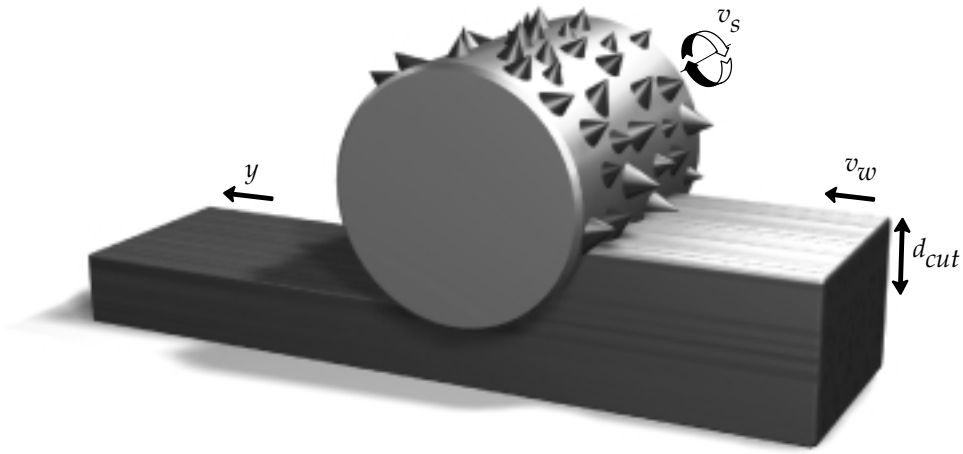

figure 2.2: *Schematic picture of the grinding wheel on the specimen.*

The grinding wheel rotates clockwise or counter clockwise in such a way that the movement of the cutting grains is in the direction of the movement of the workpiece or in opposite direction which is referred to as downward and upward grinding, respectively. Material is removed by scratching and rubbing the specimen with the abrasive grains on the grinding wheel.

2.2.2 Grinding models

This paragraph will summarise the simple models that are available from the literature to predict the roughness from the processing parameters during the grinding process. A good overview is given by Malkin [1] and Verkerk [2]. These models usually describe the chip geometry during the process. A chip is the part of material that is removed by a single abrasive grain. Based on geometrical analyses, it is possible to estimate the roughness values. However, in these models, no random distributions of abrasives are used, and therefore it is only a lower limit of the roughness predictions.

In this chapter as well as in chapter 3 only horizontal surface grinding will be considered. The basic scheme of the plane surface grinding process is depicted in figure 2.2 (see also figure 3.1). A grinding wheel of radius R_s is rotating at a peripheral velocity v_s. During the movement of the workpiece with speed v_w, a layer with thickness d_{cut} is removed from the specimen. The contact length l_c between the wheel and the workpiece can be written in terms of depth of cut and wheel radius. With the assumption that the depth of cut is much smaller than the radius of the wheel ($d_{cut} << R_s$) the relation results in

$$l_c = \sqrt{2\, d_{cut}\, R_s} \tag{2.1}$$

It should be stressed that in most figures, the depth of cut $d_{cut} \approx 10\,\mu m$ is exaggerated with respect to the radius of the wheel $R_s \approx 10\,cm$ in order to show the details of the mechanics involved in the process. In the next step the cutting path will be calculated by analysing the cutting geometry, see figure 2.3. It is assumed that all cutting grains are equally spaced on the abrasive wheel by a distance L. If all movements are translated to the grinding wheel, the assumption can be made that in successive time steps the origin (centre) of the grinding wheel moves from $O(t_0)$ to $O(t_0+dt)$. In the mean while the wheel is rotated with an angle $\theta_s=\omega_s \cdot dt = v_s \cdot dt/R_s$. The path that a single grain follows with respect to the workpiece can be described by a superposition of a translation and a circular movement. The total cutting path can mathematically be presented as a trochoid.

The distance that a grain will travel along the y-direction before a successive grain will encounter the surface of the workpiece can be written as (see also figure 2.3):

$$S = \frac{L}{v_s} v_w \tag{2.2}$$

The movements of the cutting points relative to the workpiece coordinate system *y*-*z*, i.e. the rotational and translational movements, can be split in *y*- and *z*-direction and the trochoidal path is then given by:

$$\begin{aligned} y &= R_s \sin\theta^* \pm R_s \frac{v_w}{v_s}\theta^* \\ z &= R_s\left(1-\cos\theta^*\right) \end{aligned} \tag{2.3}$$

for the horizontal *y* and vertical *z* movements, respectively, as the wheel rotates through the angle θ^*. The part in *y* after the ± sign can be seen as the distance that the wheel is moving along the *y*–direction during the time that it rotates through the angle θ^*.

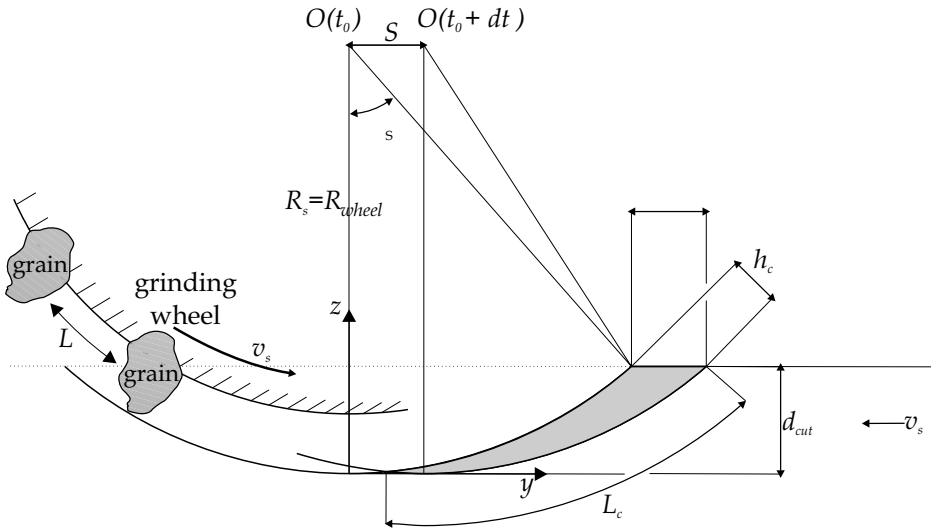

figure 2.3: *Schematic of the undeformed chip geometry.*

A grain on the grinding wheel rotates with velocity v_s. In the same time the workpiece is moving with a velocity v_w. If all movements are translated to the grinding wheel, the assumption can be made that in successive time steps the origin of the grinding wheel moves from $O(t_0)$ to $O(t_0+dt)$. In the meanwhile the wheel is rotated with an angle $\theta_s=\omega_s \cdot dt=v_s \cdot dt/R_s$. Note that the depth of cut in the figure is exaggerated with respect to the radius of he wheel!

If the speed of the workpiece is much smaller than the rotational speed of the grinding wheel ($v_w << v_s$), the angle θ^* is very small and $\sin\theta^*$ can be approximated by θ^* and $\left(1-\cos\theta^*\right) \approx \theta^{*2}/2$ using a series expansion. Finally, the trochoidal cutting path can be approximated by a parabola, relative to a Cartesian system with z-axis vertical and y-axis horizontal and results in equation (2.4).

$$z(y) = \frac{y^2}{2\ R_s\left(1 \mp \frac{v_w}{v_s}\right)^2} \tag{2.4}$$

with R_s the radius of the grinding wheel, v_w the speed of the workpiece, v_s the speed of the grinding wheel and y, z the coordinates as defined in figure 2.3. The error that is made by this simplification depends on the turning direction of the wheel and is negligible if the wheel speed v_s is much higher than the speed of the workpiece v_w. For up-grinding (+ sign), the real curvature is bigger than the wheel radius and smaller than the wheel for down-grinding (- sign).

Roughness along the grinding direction

The ideal surface roughness along the grinding direction can be determined by further elaboration on the basic grinding model and cutting geometry. The peak to valley roughness R_t can be calculated when the depth of cut is larger than the expected roughness value ($d_{cut} > R_t$). Additionally, the assumption is made that all material that an abrasive grain encounters on its path is removed from the workpiece, i.e. there is no pullout or pile-up at the side of the grooves. The spacing s between the ridges that are formed by successive grains, as indicated in figure 2.4, is given by equation (2.2). R_t can be calculated using the formulation of the cutting profile in equation (2.4). The profile has a maximum at $y=s/2$ and the relation between the peak to valley roughness and the processing parameters is then readily derived:

$$R_t = z\left(\frac{s}{2}\right) = \frac{L^2}{8R_s\left(\frac{v_s}{v_w}+1\right)^2} \tag{2.5}$$

When the speed of the grinding wheel is much higher than the infeed of the workpiece (v_s>>v_w), which is usually the case in normal grinding operations, equation (2.5) can be reduced to:

$$R_t = \frac{1}{8}\left(\frac{v_w \quad L}{v_s \quad \sqrt{R_s}} \right)^2 \tag{2.6}$$

Using an equation for the calculation of R_a, explained in more detail in next paragraph, the arithmetic roughness can be calculated by integrating equation (2.4) (notice that again the assumption (v_s>>v_w) is made), and finally this results

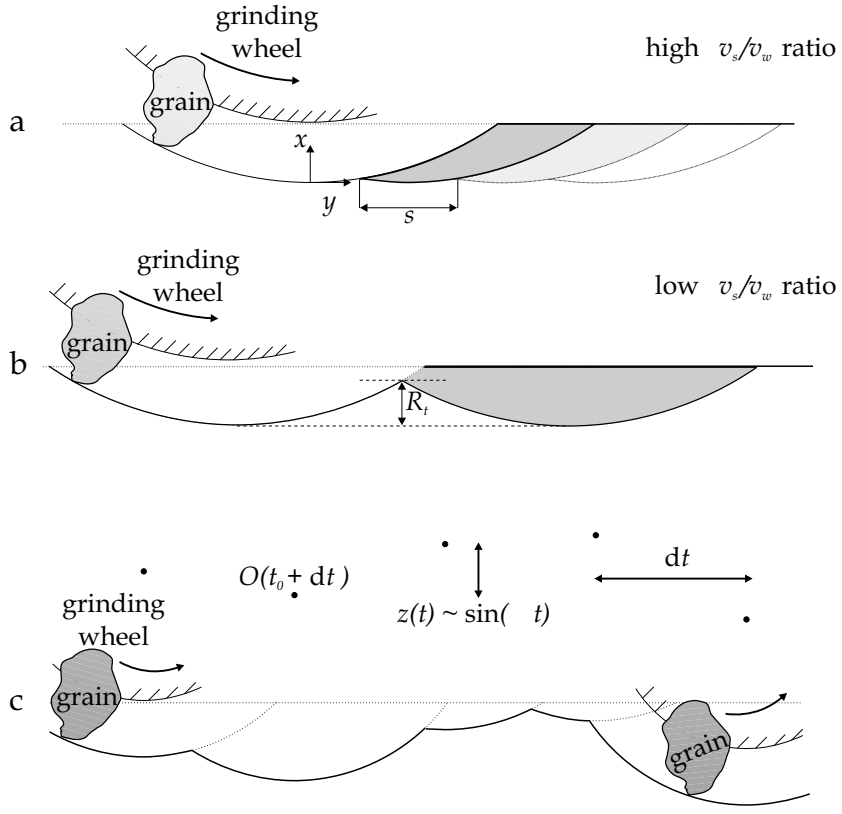

figure 2.4: *The roughness formation during the grinding process.*

The ratio between the speed of the grinding wheel v_s and the speed of the workpiece v_w determines the undeformed chip thickness and therefore the roughness along the grinding direction. ***a:*** *low v_w/v_s ratio and therefore small R_t value.* ***b:*** *high v_w/v_s ratio.* ***c:*** *surface profile along the grinding direction like in* ***a*** *but now with random grain sizes and machine vibrations.*

in:

$$R_a = \frac{1}{18\sqrt{3}}\left(\frac{v_w}{v_s}\frac{L}{\sqrt{R_s}}\right)^2 \tag{2.7}$$

From equations (2.6) and (2.7) the conclusion can be drawn that the ratio between the velocity of the workpiece and the speed of the grinding wheel v_w/v_s, and the average grain spacing L on the wheel are mainly dominating the formation of roughness during the grinding process. However, so far some aspects are not properly addressed in the one-dimensional model. First of all the cutting points are randomly distributed on the grinding wheel and secondly also the height of the cutting grains is distributed randomly. This random height distribution and supplementary vibrations of the grinding wheel will have a serious influence on the ideal roughness values as shown in figure 2.4c. In addition, no materials properties or specific material removal behaviour, such as chipping, cracking etc. is included, which may have a serious influence on the roughness values (as is shown in chapter 4 and 5).

Roughness perpendicular to the grinding direction

Roughness in the traverse direction to the grinding direction can be calculated using a similar analysis. Often the roughness traverse to the grinding direction is found to be somewhat higher than along the grinding direction. The typical wavelengths found on the surfaces are usually in both directions different: the wavelength in the grinding direction is generally longer. The roughness traverse to the grinding direction has been modelled by many researchers [3-8]. Bhateja [7] used an approach where he started with n profiles measured perpendicular to the grinding direction on the grinding wheel, i.e. in the x-direction. By overlaying i of such profiles as shown in figure 2.5, where i is depending on the processing conditions, a new resulting profile can be obtained by minimizing the summation. The surface is then progressively smoothed by the successive wheel profiles i. An empirical relationship is then obtained:

$$R_a = \frac{R_0}{i} + R_\infty \tag{2.8}$$

where i is the number of profiles and R_0 is the average roughness value of a single profile. R_∞ is the lowest roughness that can be obtained, using a specific grinding wheel, when an infinite number of profiles of the wheel encounters the surface, $i \to \infty$. The value R_∞ depends on the morphology of a grinding wheel ($R_\infty > 0$). The number i can be calculated using the spacing L between the profiles, the contact length L_e between the grinding wheel and the workpiece and accounting for the speed of the wheel and workpiece. The first choice for the arc length would be the contact length $L_c = \sqrt{2R_s d_{cut}}$ from equation (2.1). However, from figure 2.5 it can be concluded that the depth of cut d_{cut} does not affect the ideal surface roughness. Therefore, a better option for the arc length L_e is to use $L_e = \sqrt{2R_s R_t}$, where the peak to valley roughness R_t is used instead of the depth of cut d_{cut} [3]. The number of profiles is then:

$$i = \frac{v_s}{v_w}\frac{L_e}{L} = \frac{v_s}{v_w}\frac{\sqrt{2R_s R_t}}{L} \tag{2.9}$$

Using the fact that the arithmetic roughness is a fraction of the peak to valley

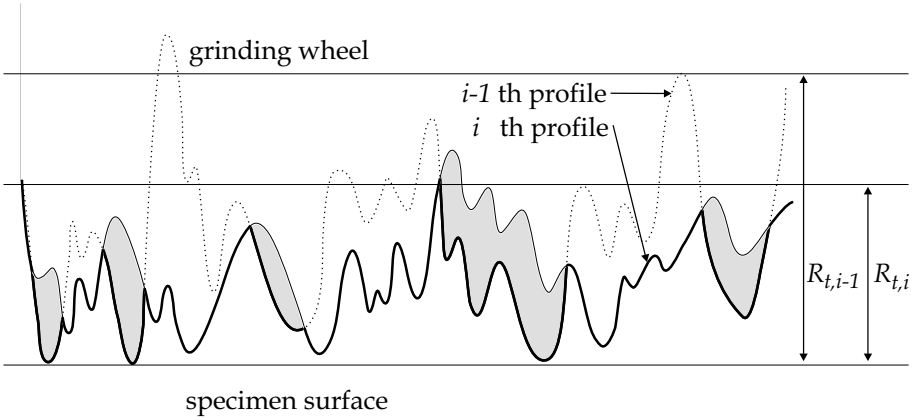

figure 2.5: *The enveloping profile model after Bhateja [7].*

Model for the prediction of the surface roughness perpendicular to the grinding direction. The profile can be determined by the cumulative grinding action of successive, perpendicular profiles of the grinding wheel. The number of profiles 1<i<n depends on the grinding parameters. The gray shaded area is the part of material that has been removed by the i-1th profile. The bold line denotes the resulting surface profile after i-profiles.

roughness, i.e. $R_t = mR_a$ with m>1, then within a practical range of the surface roughness, the average surface roughness R_a can be approximated by [1]:

$$R_a \approx \frac{R_0}{\sqrt{m}}\left(\frac{v_w}{v_s}\frac{L}{\sqrt{2R_s}}\right)^{0.8} + R_\infty \tag{2.10}$$

Again, the roughness depends on the ratio of the velocities.

2.2.3 Roughness analysis

The measurement of surface texture is often divided in three parts: surface roughness, waviness, i.e. the long wavelengths, and overall shape of the object. The surface roughness can be analysed using techniques like atomic force microscopy and stylus profilometry or the non-contacting methods like laser-profilometry and confocal microscopy. It is well known that the surface texture changes when different kinds of surface processes are applied. In order to quantify these changes well-defined parameters should be chosen [9].

The most common roughness parameters that are used thoughout this study are the arithmetric average R_a, the root mean square roughness R_q and the maximum peak to valley height R_t. These standard roughness parameters are defined as follows:

$$\begin{aligned} R_a &= \frac{1}{L_x}\int_0^{L_x}\left|z(x)-\overline{z(x)}\right|dx \approx \frac{1}{N_x}\sum_{i=1}^{N_x}\left|z_i-\overline{z}\right| \\ R_q^2 &= \frac{1}{L_x}\int_0^{L_x}\left(z(x)-\overline{z(x)}\right)^2 dx \approx \frac{1}{N_x}\sum_{i=1}^{N_x}\left(z_i-\overline{z}\right)^2 \end{aligned} \tag{2.11}$$

where L_x is the profile length and z the height fluctuation as a function of position x. $\overline{z}$ is the average of all height values: $\overline{z} = (1/L)\int_0^L z\,dx$ but more often the mean line is chosen for $\overline{z}$ by which the roughness values are corrected for inclined surfaces. The skewness R_{sk} and the kurtosis R_{ku}, which are the third moment and fourth moment of the roughness, respectively, are used to illustrate deviations of the height distribution relative to a Gaussian height distribution. The skewness is used to show asymmetry in the height distribution, i.e. for negative skewness R_{sk}<0 the distribution has a long tail at the negative side of the histogram relative to a Gaussian distribution. The

kurtosis represents the peakedness of the distribution (R_{ku}=3 is Gaussian, R_{ku}<3 broader than Gaussian distribution).

The bearing curve, after Abbott [10], is essentially the cumulative height distribution where the horizontal axis is the bearing area (%) and the vertical axis is the surface height. The bearing curve can be written as:

$$P(z \geq h) = \int_{h}^{\infty} p(z)dz \tag{2.12}$$

where *p(z)* is the normalised height distribution.

Different rough surfaces may have the same height distribution *p(z)* and R_a values because most of the parameters described above are only sensitive for the height fluctuations and not for spatial frequency at which the height fluctuations takes place, i.e. in most roughness parameters the lateral spacing is not included. Therefore the surface is analysed using the height-height correlation function *G(r)* in equation (2.13) and from this curve the Hurst exponent H, $0 \leq H \leq 1$, and the correlation length ξ can be determined [11,12]. The Hurst exponent H is calculated from the straight left part of the curve. The correlation length ξ is determined from the intersection of two fitted lines as shown in figure 2.6. The exponent H=1 corresponds to a rather smooth random

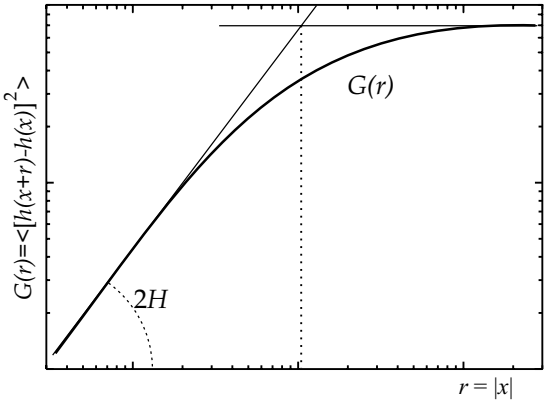

figure 2.6: *Height-height correlation function and method to determine H and ξ.*

The Hurst exponent H can be determined from the height-height correlation function G(r) by fitting a straight line to the left part of the curve. The correlation length ξ is determined from the intersection of the two fitted lines.

surface with Gaussian correlation, where for H=0 the surface is very rough and irregular. In general, H is not a direct measure of the surface roughness but rather shows how the roughness changes when the lateral length, i.e. step r along the surface, over which it is measured changes. In this analysis, it is assumed that the rough surface is a fractal up to a lateral correlation length ξ. ξ corresponds therefore to the characteristic features like ridges on the surface.

$$G(r) = \left\langle \left[h(x+r) - h(x) \right]^2 \right\rangle \approx Ar^{2H} \qquad \text{for} \quad r<\xi \tag{2.13}$$

In this equation $h(x)$ is the height fluctuation around the mean line as a function of position x, r is an arbitrary spatial distance along the x-axis, and A is a scaling factor with H the Hurst exponent. The equation shows that for $r<\xi$ the height fluctuations are correlated to the lateral distance r. In practice, the height-height correlation function is plotted versus r on a log-log scale with r varying from the sampling distance dx up to the profile length. Fitting a straight line for $r<\xi$ will yield the Hurst exponent H.

2.2.4 Materials response during the grinding process

This section is intended to provide a short overview of research developments in the material removal mechanism during abrasive processing. In particular, attention is paid to the interactions between a single abrasive grain with the workpiece. Abrasive or grooving wear can be defined as the wear due to the penetration of hard particles or surface asperities into the softer surface of the solid in sliding contact [13]. Four different wear mechanisms have been identified as presented in figure 2.7. However, during the grinding process, especially for low depth of cut, the first of these wear mechanisms, i.e. microploughing, is most likely to happen for relatively ductile materials. Depending on the materials properties, in particular the facture toughness K_{IC}, other types of material removal may occur, like in grinding ceramics, which will be discussed in more detail in chapter 5. The cumulative action of neighbouring abrasive grains may be different since the applied stress field may be different and therefore the crack growth direction or the deformation mechanism may be different.

During ideal ploughing of materials, material is continuously displaced sideways to the groove and no material is detached from the surface. However, volume loss may occur due to the action of many abrasive particles, leading to

micro-fatigue. The ridges at both sides are usually referred to as pile-up. The ratio of volume of removed material to the volume of the wear groove A_v can be quantified by a fraction f_{ab} .

$$f_{ab} = \frac{A_v - (A_1 + A_2)}{A_v} \tag{2.14}$$

For ideal ploughing f_{ab}=0, for ideal cutting the ratio f_{ab}=1 which means that all material is removed from the path that an abrasive particle encounters. When microcracking occurs, like in ceramics, f_{ab}>1. The wear mode depends on the attack angle of the abrasive particle (see figure 2.8) and the ratio between the shear strength of specimen τ and the shear strength of the abrasive particle *k*, i.e. $f_{\tau k} = \tau / k$.

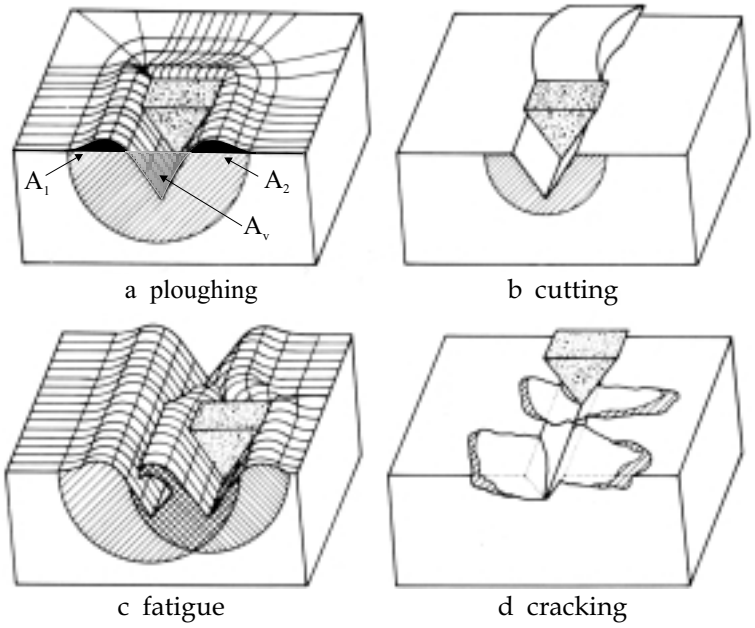

figure 2.7: *Deformation mechanisms for abrasive wear (Zum-Gahr [13]).*

The wear modes for abrasive wear: ***a:*** *ideal ploughing; material is moved sideways and there is no material loss.* ***b:*** *cutting; all material is removed from the enveloping path of the abrasive.* ***c:*** *as a result of repeated ploughing, micro-fatigue may take place.* ***d:*** *cracking may occur in brittle materials and chips of material can be removed from the specimen by brittle fracture. The total pile-up is the total area (A_1+A_2) presented in* ***a,*** *also the groove volume A_v is indicated in* ***a.***

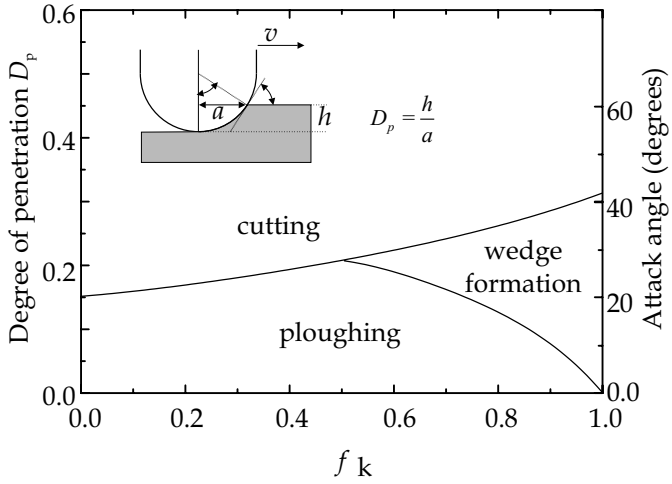

figure 2.8: *Abrasive wear modes, after Hokkirigawa [14].*

When a single abrasive particle interacts with the surface of a specimen, different wear modes can be identified. These modes depend on the attack angle θ (or degree of penetration D_p) and the shear strength of the materials involved. From the graph, it can be concluded that for attack angles higher than 45° only micro-cutting occurs.

To identify which wear mode is most likely to happen, Hokkirigawa [14,15] made a wear mechanism map [16,17]. In this map, based on empirical assumptions, the attack angle θ or degree of penetration D_p is plotted versus the ratio $f_{\tau k}$ and from the map, one can read the mode of deformation given the shear strength of the material and the type of abrasive particles. For brittle materials, the ratio $f_{\tau k}$ will in general be small, which means that cutting already starts at lower critical cutting angles. For ductile materials, the ploughing mode may first change to wedge formation where the material is moved in front of the indenter instead of sideways and then to the cutting mode at somewhat higher critical attack angles. It should be mentioned that strain rates are not considered in this basic model.

2.3 EXPERIMENTAL METHODS

In this section, the main experimental tools that were used for the grinding experiments will be explained. Equipment like scanning confocal optical microscopy, scanning electron microscopy and X-ray diffraction play a

dominant role in the analysis of ground surfaces. The use of these instruments will result in information of the surface quality in terms of morphology, roughness and residual stress state. Some other techniques were used in order to quantify the change in magnetic permeability and to quantify the number and size of (crystal) defects at the machined surface.

2.3.1 Scanning confocal microscopy

Confocal microscopy is well known from the field of (cell) biology where the technique was used to create 3D images of cells. Only recently, a growing interest in confocal microscopy appeared in the field of materials science in order to study morphology, surface roughness and phase changes in materials. The advantages of the confocal optical microscope are a higher contrast and better depth of focus compared to conventional optical microscopy. Further benefits of the confocal microscope are the enhanced lateral resolution (20%) and the possibility to record surfaces with steep surface slopes [18,19]. This instrument allows a fast and accurate 3D non-contact characterisation of engineering surfaces and therefore the roughness of ground surfaces and the profile of the grinding wheels can be studied.

The basic principle of the confocal microscope, first described by Minksy in 1957, is presented in figure 2.9 [20]. The principle works by the defocusing effect when light is reflected from a specimen: Light is emitted by a laser or a white light source and after passing the illumination pinhole and the beamsplitter (BS), the beam is focused on the specimen by the objective lens. The beam will then be reflected back through the objective lens on the beam splitter. Then the light is collimated by the confocal pinhole in the detector. The dashed lines denote the light trajectories when the specimen is not completely in focus. The light intensity of the beam through the confocal pinhole, and therefore on the detector depends on the (height) position of the focal plane. When the sample surface is out of focus part of the reflected beam will be blocked by the detector pinhole and as a result, the light intensity on the detector decreases.

The depth response $I(z)$, i.e. the intensity of light on the detector, can be written as a function of the relative position of the focal plane z, see equation (2.15) [18,21-23]. The intensity depends also on the aperture angle of the objective lens and the wavelength of radiation. The depth response has an absolute maximum when the object is exactly in focus (z=0).

$$I(z) = I_0 \left(\frac{\sin\left[k\, z\left(1-\cos(\alpha)\right)\right]}{k\, z\left(1-\cos(\alpha)\right)} \right)^2 \qquad (2.15)$$

where α is the aperture angle of the objective, $k=2\pi/\lambda$ is the wavenumber with λ the wavelength of the radiation, z the defocusing coordinate and I_0 the intensity on the detector for $z=0$. The normalised intensity versus defocusing z is plotted in figure 2.10a for a 20x objective with a numerical aperture of 0.46 and a wavelength of λ=400 nm. The aperture angle can be calculated from the numerical aperture NA using $\alpha_{\max} = \sin^{-1}(NA)/2$. Because of diffuse scattering of light, when micro-roughness is involved within the spot size, this maximum surface slope that can be measured is increased ($a_{diff}>a_{max}$). The relative height

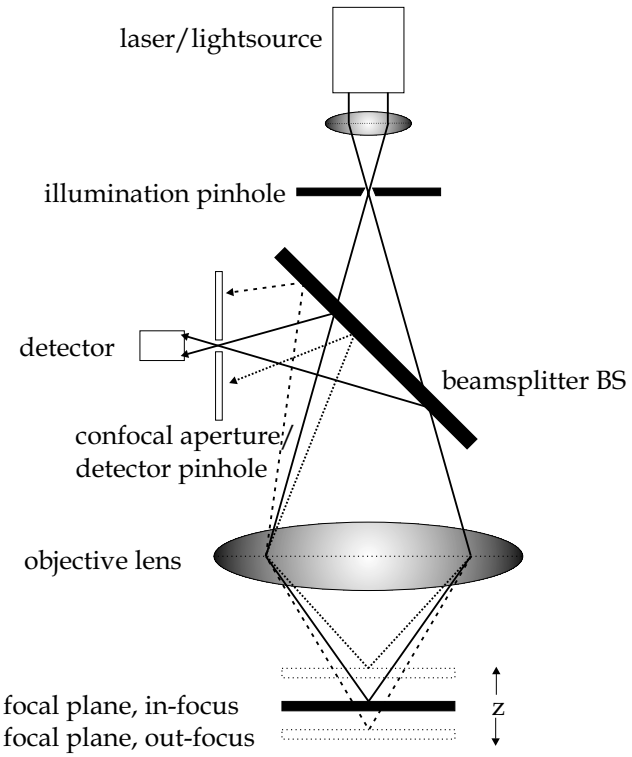

figure 2.9: *Basic principle of the confocal microscope [22].*

Light is emitted by a laser or a white light source and is passing though the illumination pinhole. After leaving the beamsplitter (BS), the beam is focused on the specimen by the objective lens. The reflected light will pass back through the objective lens on the beam splitter and is then collimated by the confocal pinhole in the detector. The dashed lines denote the light trajectories when the specimen is not completely in focus.

$h(x,y)$ of the surface can be determined from the depth response curve using the centre of gravity of the peak in equation (2.16).

$$h(x_i, y_j) = dz \frac{\sum_{z_k \in FWHM} I(x_i, y_j, z_k)\ z_k}{\sum_{z_k \in FWHM} I(x_i, y_j, z_k)} \qquad (2.16)$$

In a confocal scanning optical microscope the light beam is scanned across the surface of a specimen. For each surface point (x_i,y_j) the depth response curve is measured as explained in figure 2.10b. Then the height $h(x_i,y_j)$ of each point is calculated from this curve and a 3D surface topography is obtained.

For *x-y* scanning, a Nipkow-disk, which consists of pinholes of 20 µm arranged in a spiral way, can be used. The rotating disk is illuminated by the light from the collimator and then acts as a multiple point source. Light from each pinhole is focused on the specimen and reflected. The illumination pinhole then acts as its own detector pinhole, after which the signal is detected by a CCD camera of 512x512 pixels, see figure 2.11. The objectives are corrected for the Petzval curvature (lens aberrations) by scanning a plane mirror of quality $\lambda/10$. This curvature only depends on the optics of the measurement system. To cancel out these aberrations, the 3D image that is obtained by scanning the plane mirror is

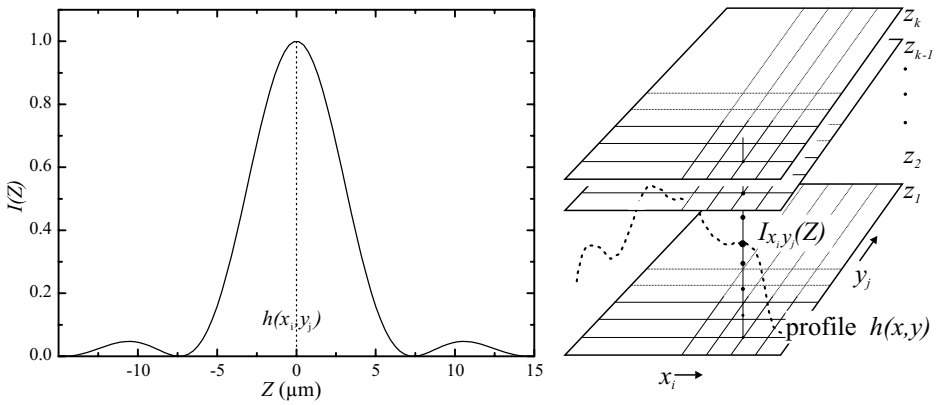

figure 2.10: *Depth response curve I(z) and scanning method.*

a: *The depth response curve is calculated from equation (2.15) using a numerical aperture NA=0.46 (objective 20x) and a wavelength of λ=400 nm. The full width at half maximum for this curve is approximately 6.5 µm.* ***b:*** *Each focal plane z_k is scanned in x and y direction. Using this method the depth response curve is measured for every surface point (x,y).*

subtracted from the actual measurements of the specimens.

In this thesis, a µSurf confocal scanning optical microscope of Nanofocus Meßtechnique GmbH was used equipped with a white light source and a Nipkow disk for scanning along the *x*-*y* plane. For the scanning of the vertical (*z*-) axis a steppermotor with a resolution of *dz*=0.1 µm or a piëzo-scanner with a resolution of *dz*=0.01 µm is used. The properties of the objectives and the corresponding resolutions are listed in appendix 2. An example of a measured 3D topography is presented in figure 2.12.

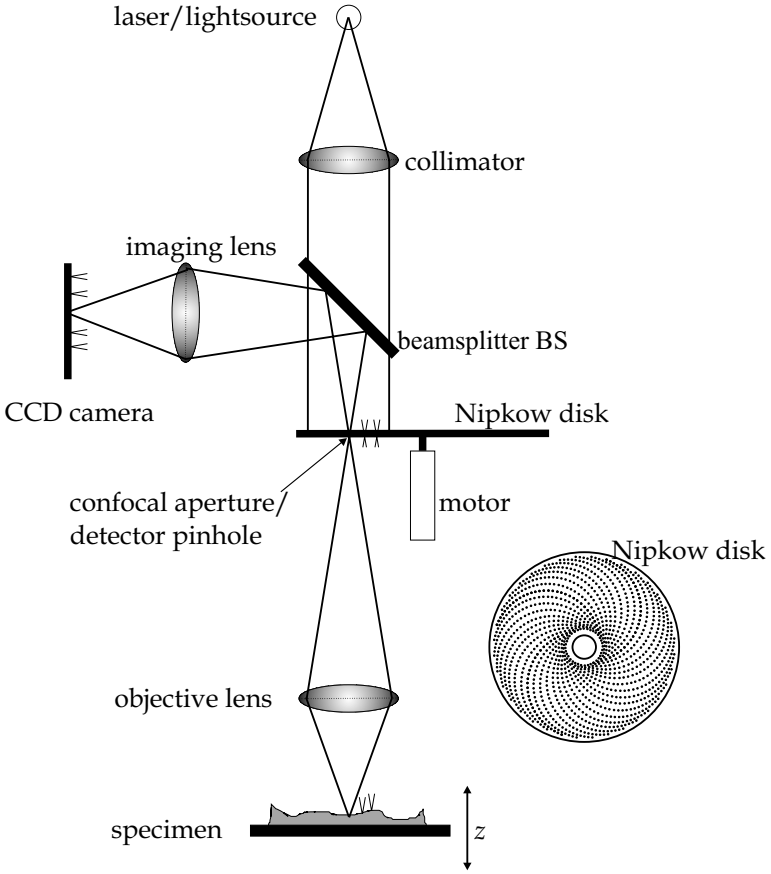

figure 2.11: *Schematic set-up of confocal scanning optical microscopy [22].*

The confocal scanning optical microscope (CSOM) based on a multiple pinhole mask (a Nipkow disk). The rotating disk is illuminated by a plane wave. The multiple-point source is focused on the specimen and then reflected back on the Nipkow disk. The multiple pinholes act as the confocal pinhole, where after the light is focused on a CDD camera.

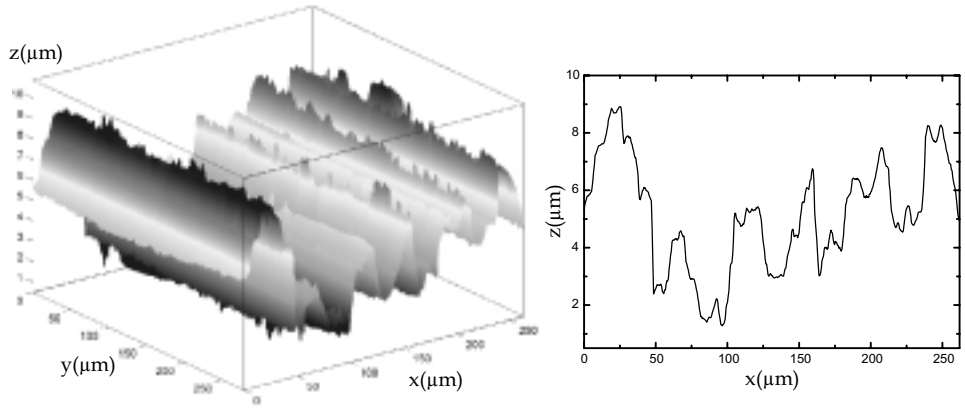

figure 2.12: *Example of a 3D topography.*

The 3D topography of ground WC-10wt%Co and the typical 2D profile perpendicular to the grinding direction using. The 50x/0.80 objective of the confocal microscope was used to record the image. From the data, the 2D and 3D roughness values are calculated.

2.3.2 Scanning electron microscopy

Electron microscopy is often used to study the surface morphology of engineering surfaces as well as for the study of cracks, metallurgical phases, microstructure and grain sizes [24]. In scanning electron microscopy (SEM) an electron beam is focused and scanned across a sample's surface. When the electrons hit the specimen, a variety of signals is generated due to the interaction of a primary electron with matter. Every signal recorded by one of the detectors gives specific information of the surface of the specimen or its chemical content.

A schematic figure of a scanning electron microscope is presented in figure 2.13. In a FEG-SEM electrons are generated by the field emission (electron) gun using a high electrostatic field. Then the electrons are accelerated with an energy between 1 keV and 30 keV down the column towards the specimen. The magnetic lenses (condensor lens and objective lenses) focus the beam to a spot with a diameter of approximately 1-10 nm on the specimen. The electron beam is swept over the surface of the sample by the scanning coils. The magnified image is formed by relating the detector signal to the position of the beam.

Secondary electrons are produced when loosely bound atomic electrons are released by the interaction with a primary electron. These secondary electrons

have a small mean free path because of the low energy they have. Therefore, the information is coming from a shallow depth (~10 nm). The signal of the backscatter electron detector is formed by the scattering of primary electrons from the electron beam with the nucleus of an atom of the material. With increasing atom number, the intensity of the backscattered electrons is increasing and hence the signal contains information on chemical composition. Because of the higher escape depth (~1 µm) of backscattered electrons the resolution of the image is not as good as for the secondary electrons.

Energy dispersive spectroscopy (X-ray microanalysis) and Auger electron spectroscopy are closely related since both start when a primary electron ejects a core electron from its shell. In X-ray microanalysis, this ejected electron will be replaced by an electron from an outer shell, emitting an X-ray photon with a characteristic energy. Measuring the energies of the X-ray photons will yield the chemical composition of the material up to a depth of 10 µm depending on the

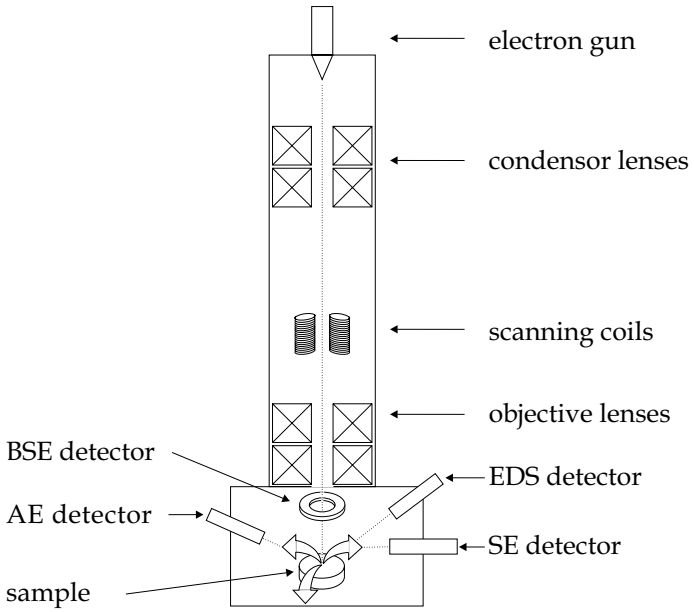

figure 2.13: *Schematic picture of the scanning electron microscope.*

Electrons, that are generated by the field emission gun are accelerated with an energy between 1 keV and 30 keV and focused by the electromagnetic lenses onto the sample. The signals that are emitted from the sample are detected by a variety of detectors such as secondary electron (SE), backscattered electron (BSE), Auger Electron (AE) detectors and an energy dispersive spectrometer (EDS).

acceleration voltage. In Auger electron spectroscopy (AES), this X-ray photon will be absorbed by an electron in an outer shell of the atom. This electron with a characteristic energy is then emitted. This energy is specific for a certain element and gives some information on the binding energies of the atom. The detected electrons are ejected from a depth up to 1 nm.

In this study a Philips XL30 FEG-SEM equipped with a secondary electron detector, a backscattered electron detector and an energy dispersive X-ray spectrometer was used to study the microstructure and morphology of the materials before and after grinding. A scanning Auger electron microscope (SAM) of JEOL (JAMP 7800F) with a base pressure of $5 \cdot 10^{-8}$ Pa and a beam spot size of 20 nm was applied to reveal the composition in the grinding process deformed surface layer. Surface cleaning to remove contaminants was performed by in-situ ion sputtering with 3 keV Ar^+ ions.

2.3.3 X-ray diffraction and residual stress measurements

X-ray diffraction is employed to examine the residual strains in the subsurface of the ground specimens. The $\sin^2\psi$ method is used to measure the strains in the specimens before and after grinding. The residual stress is calculated from the measured strains. The X-ray diffractometer is set up to measure the strains perpendicular to the grinding direction, i.e. φ=90°.

X-rays are reflected from certain crystallographic planes in a specimen. This phenomenon can be described by a rather simple equation, which is known as Bragg's law as shown in equation (2.17):

$$2 \; d_{hkl} \; \sin\theta = n\,\lambda \qquad (2.17)$$

where d_{hkl} is the distance between the (hkl) planes, λ is the wavelength of the X-rays ($\lambda_{K\alpha1,Cu}$=1.54060 Å) and θ is the diffraction angle. Usually the first order diffraction is taken, n=1. Bragg reflection can occur only for wavelengths $\lambda \leq 2d$. For each planar distance and hence crystallographic direction, the diffraction angle θ is different.

If an elastic strain is applied to a (poly) crystalline material by a certain stress, the lattice spacings in this material are changed from its stress-free distance d_0. In X-ray residual stress measurements, this change in lattice spacing is determined from the shift in the diffraction peak for a specific crystallographic

direction using Bragg's law defined in equation (2.17) and see figure 2.14 [25-27]. This shift in lattice spacing can be related to the stress using Hooke's law.

The strain $\varepsilon^{lab}_{33,\phi\,\psi}$ can be written in terms of lattice spacing and is then transformed from the laboratory system to the system of the specimen, see figure 2.15. After applying Hooke's law, assuming linear elasticity, the relation between the measured spacings $d_{\phi\psi}$ and the stress components σ_{ij} is given by:

$$\begin{aligned}\frac{d_{\phi\varphi}-d_0}{d_0}=\varepsilon^{lab}_{33,\phi\psi}= \quad & \frac{1+\nu}{E}\left\{\sigma_{11}\cos^2\phi+\sigma_{12}\sin 2\phi+\sigma_{22}\sin^2\phi-\sigma_{33}\right\}\sin^2\psi \\ & +\frac{1+\nu}{E}\sigma_{33}-\frac{\nu}{E}\left\{\sigma_{11}+\sigma_{22}+\sigma_{33}\right\} \\ & +\frac{1+\nu}{E}\left\{\sigma_{13}\cos\phi+\sigma_{23}\sin\phi\right\}\sin 2\psi\end{aligned} \tag{2.18}$$

If the stress state is biaxial, which is a reasonable assumption because the stress perpendicular to a free surface is always zero at the surface and hence the in-plane stress components are the only components that are non-zero ($\sigma_{11}\neq 0$, $\sigma_{22}\neq 0$), then equation (2.18) can be simplified to:

$$\frac{d_{\phi\psi}-d_0}{d_0}=\frac{1+\nu}{E}\sigma_\phi\sin^2\psi-\frac{\nu}{E}(\sigma_{11}+\sigma_{22}) \tag{2.19}$$

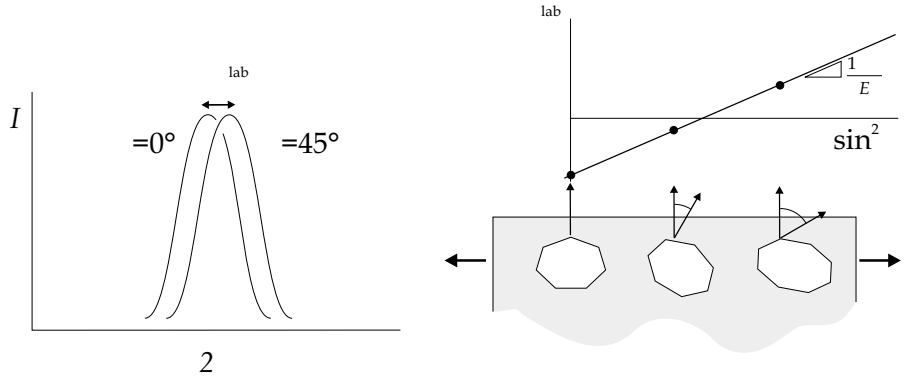

figure 2.14: *X-ray diffraction in a stressed material.*

The residual stress can be determined by X-ray diffraction. The lattice spacing of a certain crystallographic plane is measured for different ψ angles by fitting a straight line to the d versus sin²ψ plot

In this equation, E is the Young's modulus, ν is the Poisson's ratio and d_0 is the stress free plane spacing and in practice $d_0 = d_{\phi\,\psi=0}$ is chosen, which is satisfied because $d_{\phi\,\psi} - d_0 \ll d_0$ and therefore only a negligible error is made. $d_{\phi\psi}$ represents the measured lattice spacing, ψ is the angle as defined in figure 2.15 and σ_{ij} 's are the stress components. Even though the penetration depth of X-rays is usually small, the assumption that the stress components normal to the surface are negligible within the measured volume is not always valid [28]. Ψ-splitting may indicate that the shear stress components σ_{13} and σ_{23} are non-zero and more measurements are required to monitor all the stress components σ_{ij} of the triaxial stress state.

For isotropic materials, it is satisfactory to choose the macroscopic values for Young's modulus E and Poisson's ratio υ. However, it is better to use the plane specific X-ray elastic constants. In the case of an elastically isotropic material, these can be expressed as $S_1 = -\nu/E$ and $\frac{1}{2}S_2 = (1+\nu)/E$ [26]. In principle, the X-ray elastic constants can be calculated from the single crystal elastic constants using the Voigt, Reuss or some average approximation [27]. For relative comparisons of residual stress states in the same material, it is sufficient to use any arbitrary elastic constant since in this case this number will be cancelled out.

The residual stress can be determined by choosing a crystal plane with the according 2θ peak. Then the lattice spacings $d_{\phi\,\psi}$ of these planes are measured and calculated using Bragg's law for some ψ-angles. The stress σ_ϕ can be

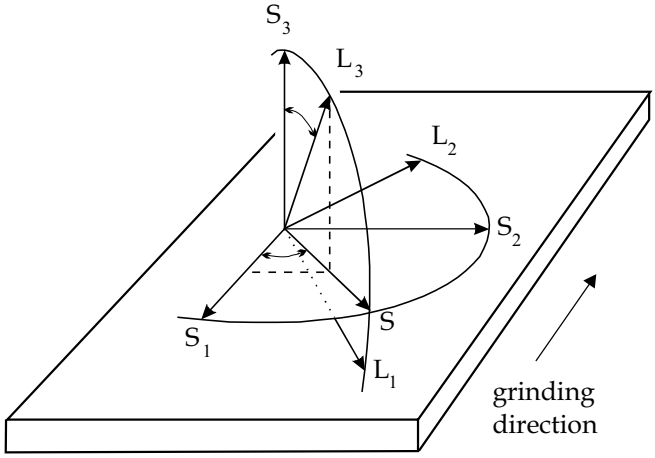

figure 2.15: *The transformation from laboratory to sample coordinates.*

The transformation from the orthogonal system of the Laboratory L_1, L_2 and L_3 to the system of the specimen S_1, S_2 and S_3. This transformation is defined by the angles ψ and the azimuth angle φ.

determined from the gradient of $d_{\phi\psi}$ as function of $\sin^2\psi$ by fitting a straight line to the $d_{\phi\psi}$ versus $\sin^2\psi$ plot as shown in figure 2.14.

2.3.4 Additional experimental methods

In this section, a brief summary is given of other experimental techniques that were used to study the surface quality of the ground materials.

Positron annihilation

Positrons can be used as a non-destructive tool to study materials defects [29-31]. The specific types of defects that can be studied by probing with positrons are vacancies and voids, the so-called volume defects. When a positron is trapped somewhere in the material, the positron will annihilate with an electron from the vicinity. After the annihilation of a positron with an electron, two 511 keV γ-photons will be emitted. The spread around the 511 keV energy peak contains information of the local electron density and by measuring the Doppler broadening of this peak the distribution and density of defects can be quantified. Two parameters *S* and *W* are often used to describe the broadening of the detected energy peak [32]. *S* is the fraction of energy close to the maximum of the peak relative to the total integrated area of the peak T where *W* is the fraction of the tails, see figure 2.16. *S* corresponds to the annihilation with conducting electrons and therefore *S* can be seen as the density of free electrons. Notice that for metals, *S* is increasing with increasing defect density since more free electrons are available at a defect. *W* measures the annihilations with core shell electrons and is thus more sensitive for the bulk of the material. In addition, positron lifetime measurements were performed. With this technique, the time difference between the emission and the annihilation is measured. The typical lifetime in bulk materials (100-200 ps) is shorter than the time for defects, where the lifetimes may increase up to 500 ps depending on the size of the defect. If the open volume of the defects is large enough, like in clusters of voids and (micro) cracks, positronium P_s might be formed, accompanied by a long lifetime. A schematic picture of the interaction of a positron beam with a material is shown in figure 2.16.

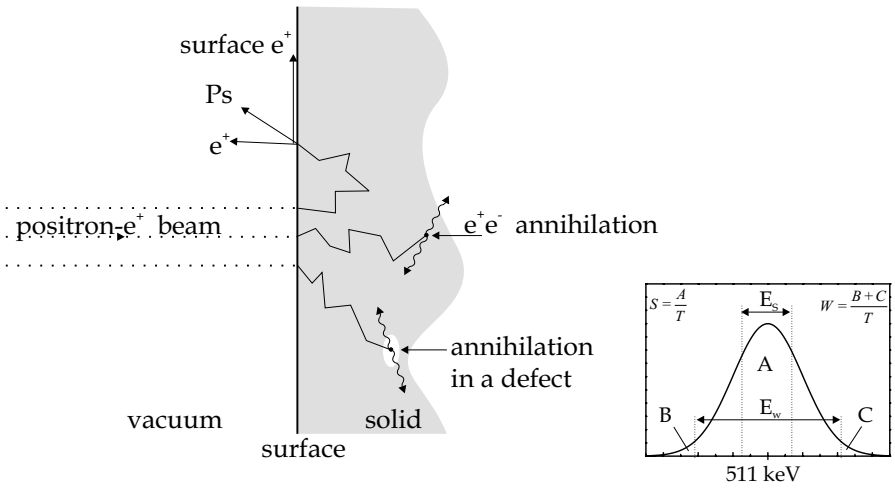

figure 2.16: *Interaction of positrons with a material and the definition of S and W.*

The interaction of a positron beam e^+ with a material: the positrons can move through the material by thermal diffusion. When a positron is trapped, it will annihilate with an electron, emitting two 511 keV γ-photons. The positron has a higher probability of annihilation with core electrons in the bulk than with core electrons in open volume defects. For the probability with free electrons, the opposite is true. (T is the total integrated area of the peak)

Magnetic measurements

Magnetic measurements were performed by applying a magnetic field to a specimen. The magnetic response of the material was measured using a conventional bridge circuit at 4 kHz, 75 mV. The magnetic permeability was determined from the hysteresis loop and was measured at different temperatures from 0 °C up to the Curie temperature.

REFERENCES

1. S. Malkin, Grinding technology: theory and applications of machining with abrasives, Society of Manufacturing Engineers (SME), Michigan, 1989
2. J. Verkerk, Wheelwear control in grinding, Thesis of the University of Delft, 1976
3. J. Peklenik, *Journal of Engineering for Industry*, **86** 85-94 (1964)
4. H. Yoshikawa, T. Sata, *Annals of the CIRP*, **16** 297-302 (1968)
5. S.S. Law, S.M. Wu, A.M. Joglekat, *Journal of Engineering for Industry*, **95** 983-991 (1973)
6. S.M. Pandit, P.T. Suratkar, S.M. Wu, *Wear*, **39** 205-217 (1976)

7. C.P. Bhateja, *Annals of the CIRP*, **25** (1) 333-337 (1977)
8. M. Hasegawa, *Journal of Engineering for Industry*, **103** 22-32 (1981)
9. T.R. Thomas, Rough surfaces, Longman, London, 1982
10. E.J. Abbott, F.A. Firestone, *Mechanical Engineering*, **55** 569-572 (1933)
11. P. Meakin, Fractals, scaling and growth far from equilibrium, Cambridge nonlinear science series 10, Cambridge university press, Cambridge, 1998
12. Y.P. Zhao, G.C. Wang, T.M. Lu, Characterisation of amorphous and crystalline rough surfaces – principles and applications, Experimental methods in the physical science, vol 37, 2000
13. K.H. Zum-Gahr, Microstructure and wear of materials, Elsevier, Amsterdam, 1987
14. K. Hokkirigawa, K.Kato, *Tribology International*, **21** (1) 51-57 (1988)
15. K. Hokkirigawa, T. Kato, T. Fukuda, M. Shinooka, *Wear*, **214** 192-201 (1998)
16. K.H. Zum-Gahr, *Tribology International*, **31** (10) 587-569 (1998)
17. J.A. Williams, *Wear*, **225-229** 1-17 (1999)
18. T. Wilson, Confocal microscopy, Academic Press, San Diego, 1990
19. A. Frank, *Nanotechnology*, **2** 11-18 (1991)
20. M. Minsky, Microscopy apparatus, USA patent 3013467 (filed 1957), 1961
21. C.J.R. Sheppard, S.M. Shotton, Confocal laser scanning microscopy, Springer-Verlag, New York, 1997
22. H.J. Jordan, M. Wegner, H. Tiziani, *Measurement Science and Technology*, **9** 1142-1151 (1998)
23. G. Udupa, M. Singaperumal, R.S. Sirohi, M.P. Kothiyal, *Measurement Science and Technology*, **11** 305-314 (2000)
24. J.I. Goldstein, D.E. Newbury, P. Echlin, D.C. Joy, C. Fiori, E. Lifshin, Scanning electron microscopy and X-ray microanalysis, Plenum Press, New York, 1984
25. B.D. Cullity, Elements of X-ray diffraction, Addison-Wesley, London, 1978
26. I.C. Noyan, J.B. Cohen, Residual stress: measurement by diffraction and interpretation, Springer-Verlag, Berlin, 1987
27. B. Eigenmann, E. Macherauch, *Materialwissenschaft und Werkstofftechnique*, **26** 148-160 and 199-214 (1995)
28. G. de With, N. Sweegers, *Wear*, **188** 142-149 (1995)
29. P. Asoka-Kumar, K.G. Lynn, D.O. Welsh, *Journal of Applied Physics*, **76** 4935- (1994)
30. R.A. Hakvoort, A. van Veen, J. Noordhuis, J.Th.M. de Hosson, *Surface and Coatings Technology*, **66** 393-397 (1994)
31. L.V. Jørgensen, A. van Veen, H. Schut, *Nuclear Instruments and Methods in Physics research B*, **119** 487-490 (1996)
32. A. van Veen, H. Schut, P.E. Mijnarends, *Depth-profiling of subsurface regions, interfaces and thin films*, in: Positron beams and their applications, ed. P.G. Coleman, World Scientific, 191-225 (2000)

APPENDIX 2: OBJECTIVE PROPERTIES OF THE CONFOCAL MICROSCOPE

table 2.1: *The properties of the different objectives (OLYMPUS) used in the confocal scanning optical microscope*

Objective type	10x/0.30	20x/0.46	50x/0.80	100x/0.95
measurement field (µm x µm)	1400x1320	700x660	280x264	140x132
numerical aperture	0.30	0.46	0.80	0.95
max. surface slope (°)	8.7	13.7	26.6	35.9
working distance (mm)	10.1	3.1	0.66	0.31
vertical resolution (nm)	>50	>40	>20	>5
lateral resolution (µm)	2.59	1.29	0.55	0.27